# A High Performance Quasi-Solid-State Supercapacitor Based on CuO Nanoparticles with Commercial-Level Mass Loading on Ceramic Material $La_{1-x}Sr_xCoO_{3-\delta}$ as Cathode

Peipei Liu[a,b], Xiaolin Weng[a], Zhijun Liu[a], Yapeng Zhang[a], Qianyuan Qiu[a], Wei Wang[a], Mingyang Zhou[a], Weizi Cai[b], Meng Ni[b,*], Meilin Liu[a,c], Jiang Liu[a,*]

[a] *Guangzhou Key Laboratory for Surface Chemistry of Energy Materials, New Energy Research Institute, School of Environment and Energy, South China University of Technology, Guangzhou 510006, China.*

[b] *Building Energy Research Group, Department of Building and Real Estate, The Hong Kong Polytechnic University, Hung Hom, Kowloon, Hong Kong, China.*

[c] *School of Materials Science and Engineering, Georgia Institute of Technology, 771Ferst Drive, Atlanta, GA 30332-0245, USA.*

*Corresponding authors:

E-mail: meng.ni@polyu.edu.hk; jiangliu@scut.edu.cn

## ABSTRACT

To evaluate the performance of supercapacitor objectively and accurately, it is critical to develop an electrode with a thickness in the hundred-micrometer range with commercial-level mass loading of the active material. In this work, for the first time CuO nanoparticles with high mass loading (~10 mg $cm^{-2}$) are supported on the $La_{1-x}Sr_xCoO_{3-\delta}$ (LSC, $0 \leq x \leq 0.8$) substrate (thickness: ~500 μm) and used as a cathode for asymmetric supercapacitor. The novel and binder-free CuO/LSC73 (i.e. $x$ = 0.3) electrode shows high areal capacitance ($C_a$) of 5.45 F $cm^{-2}$ and specific capacitance ($C_s$) of 545 F $g^{-1}$. The packaged quasi-solid-state asymmetric supercapacitor with carbon

cloth as an anode and PVA/KOH as an electrolyte, delivers an ultrahigh volumetric energy density of 4.92 mWh $cm^{-3}$ at a current density of 10 mA $cm^{-2}$ with a wide potential window of 1.4 V, which are comparable to those of lithium batteries (0.3–10 mWh $cm^{-3}$). In addition, the power density of the assembled device can reach 727 mW $cm^{-3}$ at 80 mA $cm^{-2}$ with a high energy density of 3.03 mWh $cm^{-3}$. The good electrochemical performance is attributed to high conductivity of the porous LSC73 substrate and uniform distributions of CuO nanoparticles, which are beneficial for the fast transport of electrons and diffusion of ions.

**KEYWORDS:** *Supercapacitors, Electrode, Ceramic material* $La_{1-x}Sr_xCoO_{3-\delta}$*, Commercial level CuO mass loading, High volumetric energy density*

## 1. INTRODUCTION

Supercapacitors are promising sustainable and efficient energy storage devices, because of their higher power density than batteries, and higher energy density than traditional capacitors. They also have a comparably long cycle life, fast charge/discharge rate, an ease of maintenance, and a wide operating temperature [1,2]. Though high energy densities of supercapacitors have been achieved, the mass loading of active materials on traditional substrates is only ~0.2–2 mg $cm^{-2}$ [3-5], which is far less than the required value in commercial supercapacitors (~ 10 mg $cm^{-2}$). Therefore, it is valuable to exploit novel electrodes with high mass loading of active materials to deliver a superior energy density with acceptable power density.

Generally, electrodes are composed of an active material with remarkable capacitive properties and a substrate (i.e. current collector) with high electrical conductivity [6-8]. Copper oxide has become a competitive candidate as the active

material for supercapacitors due to its abundance, low cost, lack of toxicity, and its fantastic theoretical capacitance (~1800 F $g^{-1}$) [9-11]. However, the mass loading of CuO-based materials on conventional substrates is not as high as one would wish for. For instance, Xu et al. [12] reported CuO nanoflowers (~0.32 mg $cm^{-2}$) on carbon fiber fabric that demonstrated a specific capacitance of 839.9 F $g^{-1}$ at a scan rate of 1 mV $s^{-1}$; Moosavifard et al. [13] prepared nanoporous CuO (~3.5 mg $cm^{-2}$) on Ni foam, and obtained a specific capacitance of 431 F $g^{-1}$ at 3.5 mA $cm^{-2}$. To tackle this issue, developing a novel substrate that can support CuO with commercial-level mass loading would be scientifically and commercially important.

Owing to the structural ability and high catalytic activity, perovskite oxide materials with $ABO_3$ structure, where A represents lanthanide or alkali earth element and B means a mixed valence transition metal, have been widely used as electrodes and catalysts for solid oxide fuel cells [4, 15], oxidation of volatile organic compounds [16,17], and oxygen evolution reaction [18, 19]. Moreover, the electrical properties of the perovskite materials can be improved via A or B partially substituted by aliovalent ions, producing extra holes in the valance band essentially that reduce energy band gap and increase conductivity [20, 21]. $LaCoO_3$ as one of energy conversion ceramic materials has attracted much attention, especially the strontium substituted lanthanum cobaltite $La_{1-x}Sr_xCoO_{3-\delta}$ ($0 \leq x \leq 0.8$) with its sufficient electrical conductivity (~$10–10^3$ S $cm^{-1}$) [22-24]. Mineshige et al. [25] have demonstrated the high electrical conductivity of $La_{1-x}Sr_xCoO_3$ ($0 \leq x \leq 0.7$) at temperatures from 300 K to 1473 K. Therefore, LSC with different contents of Sr could be a promising alternative substrate for supercapacitors.

Inspired by the preliminary studies on LSC, we investigated the structural and electrochemical properties of the synthesized LSC substrate in detail to find the optimal

content of Sr. CuO nanoparticles with a high mass loading of 10 mg $cm^{-2}$ directly loaded on porous LSC were prepared by simple infiltration and calcination process. The novel electrode CuO/LSC73 displays both high specific capacitance of 545 F $g^{-1}$ and areal capacitance 5.45 F $cm^{-2}$ at 1 mA $cm^{-2}$. Additionally, a quasi-solid-state asymmetric supercapacitor composed with CuO/LSC73 as the cathode, a carbon cloth as an anode and a PVA/KOH as a gel electrolyte showed excellent capacitive performance with high volumetric energy density of 4.92 mWh $cm^{-3}$ and long cycle life (~98% retention of initial capacitance after 3500 cycles at 50 mA $cm^{-2}$). We also used the two quasi solid-state devices in series as a power source for LED to validate its possible application in practice.

## 2. EXPERIMENTAL SECTION

$La_2O_3$, ethanol, starch (as pore former) and polyvinyl butyral were bought from Sinopharm Chemical Reagent Co., Ltd. $SrCO_3$ and $Co_3O_4$ were purchased from Guangzhou Chemical Reagent Co., Ltd and Aladdin Chemical Co., Ltd, respectively. Carbon fiber paper (CFP) was purchased from Shanghai hesen electric Co., Ltd. $Cu(NO_3)_2{\cdot}3H_2O$ was purchased from Tianjindamao Chemical Reagent Co., Ltd. All these reagents were of analytical grade. A carbon cloth wafer with a diameter of 1.00 cm and thickness of 0.02 cm was bought from Shanghai hesen electric Co., Ltd, and was pre-calcined in air for 2 h at 400 °C.

### 2.1 Synthesis of porous ceramic material LSC

The porous ceramic material $La_{1-x}Sr_xCoO_{3-\delta}$ ($x$=0, 0.2, 0,3, 0.4, 0.5, 0.6, 0.8) were synthesized using a solid-state method reported previously by our group [26], and denoted as LCO, LSC82, LSC73, LSC64, LSC55, LSC46 and LSC28, respectively. The detailed steps for preparation of the $La_{1-x}Sr_xCoO_{3-\delta}$ substrate are as followings: (I)

$La_2O_3$ as one of raw materials, was pretreated by calcination at 1000 °C for 2 h; (II) Based on the stoichiometric amount, the pre-calcined $La_2O_3$ was mixed with $SrCO_3$ and $Co_3O_4$ through ball milling for 8 h, using ethanol as solvent; (III) Polyvinyl butyral (3wt.%, as binder) was added into the mixture, and then grinded for 30 min; (IV) The mixture was dried and pressed into pellets, employing a stainless steel mold (Diameter: 13 mm); (V) The pellets were fired at 1100 °C for 12 h to get the desired products. The diameter, thickness and average weight of the pellets were 1.16 cm, 0.05 cm and 0.150 g, respectively. The porosity of the LSC substrate was ~38%, according to the Archimedes' method [27].

### 2.2 Preparation of CuO nanoparticles loaded on LSC

CuO nanoparticles were loaded on LSC73 through infiltration and calcination in two simple steps. First, the porous LSC73 pellets were submerged in a 0.5 M $Cu(NO_3)_2$ solution for 20 s and then dried in a vacuum drying oven for 20 min at 120 °C. This process was repeated to obtain the required mass loading of CuO on LSC73. After that, the samples were calcined for 1 h at 500 °C in a gaseous argon atmosphere to obtain the CuO/LSC73 electrode.

### 2.3 Characterization

The crystallinity, morphology and structure of the products were examined using X-ray diffraction (XRD, Bruker D8 Advance diffractometer with Cu Kα ($\lambda$ = 0.15418 nm), field emission scanning electron microscope (Merlin, 5.0 kV) and transmission electron microscopy (TEM, JEOL JEM-2100). X-ray photo spectroscopy (XPS, Escalab 250, Al Kα) was employed to identify the elemental compositions and the chemical states of the prepared samples. Nitrogen adsorption-desorption measurement was carried out to examine the porous structure of the CuO/LSC73 electrode.

## 2.4 Electrochemical measurements

Electrical conductivities of the porous $La_{1-x}Sr_xCoO_{3-\delta}$ were evaluated by the four-point method, using Ag paste and Ag thread as a current collector and a conductive wire, respectively. In addition, to investigate the capacitive performance of the prepared electrode (as a working electrode), a cell in a standard three electrode system was tested in 3.0 M KOH solution using a CHI600E (Shanghai Chenhua) electrochemical station. The Pt mesh (1 $cm^2$) and Hg/HgO were used as counter and reference electrodes, respectively. Cyclic voltammetry (CV) profiles were recorded from −0.3 to 0.4 V at various scan rates. Galvanostatic charge-discharge (GCD) curves were studied at different current densities between −0.1 and 0.4 V. Electrochemical impedance spectra (EIS) were carried out in the frequency range from 0.01 to 10 MHz.

A quasi-solid-state asymmetric supercapacitor (CuO/LSC//carbon cloth) was assembled, employing a cellulose paper as the separator and PVA/KOH gel as the electrolyte. The total thickness, weight and volume of the designed quasi solid-state device were 0.07 cm, 0.162 g and 0.074 $cm^3$, respectively. The electrochemical properties were recorded under a wide voltage of 1.4 V. The capacitance ($C$), energy density ($E$) and power density ($P$) of the single electrode and assembled device were evaluated according to the following equations [28]:

$$C = \frac{2i\int Vdt}{V^2|_{Vi}^{Vf}} \qquad (1)$$

$$E = \frac{1}{2}CV^2 \qquad (2)$$

$$P = \frac{E}{t} \qquad (3)$$

where C (F $cm^{-2}$ or F $g^{-1}$), i (mA $cm^{-2}$) and V (V) represent the capacitance, the current

density, and the potential window, respectively. $V_i$ and $V_f$ mean final window and initial window, respectively. t (s) is the discharge time. E (mWh $cm^{-3}$) and P (mW $cm^{-3}$) are the volumetric energy density and power density, respectively.

## 3. RESULTS AND DISCCUSSION

Fig. 1 (a) shows XRD patterns of the $La_{1-x}Sr_xCoO_{3-\delta}$ at wide 2θ degree range from 20º to 80º, confirming the successful synthesis of the perovskite oxide phase. The more intense diffraction peaks shift to left with the increase of *x*, which can be seen clearly from the enlarged angle between 32 º and 34 º in Fig. 1(b). Moreover, there are two wide peaks when the amount of Sr (*x*) is less than or equal to 0.5, while relative sharp peaks are observed when $x > 0.5$. The tendency can be explained by the distortion in the crystal structure. LCO without Sr substitution (i.e. $x = 0$) possesses a rhombohedral structure corresponding to the standard patterns of $LaCoO_3$ (JCPDS. no. 84-0848). However, the crystal structures transfer from rhombohedral to cubic units gradually as the value of *x* increases. This is an effect of the larger ionic radius of $Sr^{2+}$ (1.18 Å) as compared to $La^{3+}$ (1.03 Å) [29, 30]. The detailed crystallographic parameters of the materials are presented in Table. 1.

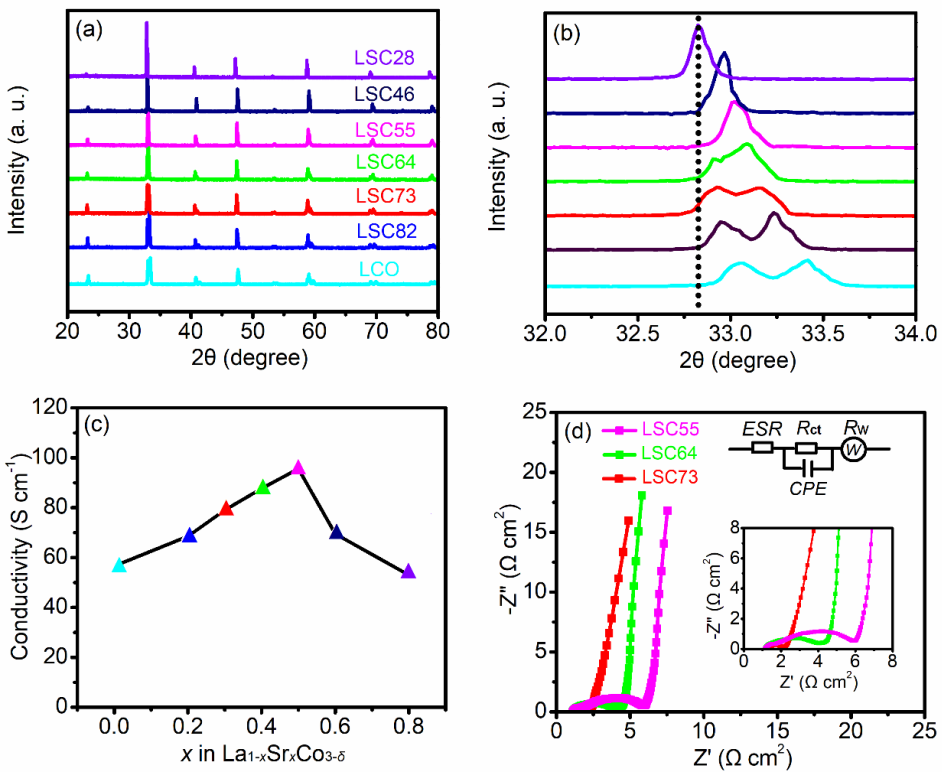


**Figure 1. (a and b) XRD patterns and (c) electrical conductivities of the prepared $La_{1-x}Sr_xCoO_{3-\delta}$ ($0 \leq x \leq 0.8$); (d) EIS plots of the LSC55, LSC64, LSC73.**

The electrical conductivities of the synthesized porous $La_{1-x}Sr_xCoO_{3-\delta}$ at room temperature are displayed in Fig. 1(c). The orders are LSC55 > LSC64 > LSC73 > LSC46 > LSC82 > LCO > LSC28. In other words, when $La^{3+}$ is partially substituted by the larger ion $Sr^{2+}$, an increase in electrical conductivity is observed with *x* varying from 0.0 to 0.5, which may be attributed to the increased overlap of the Co(3d)-O(2p) band and oxidation of $Co^{3+}$ to $Co^{4+}$ [29, 31]. Nevertheless, when the $Sr^{2+}$ contents exceed 0.5, large amounts of oxygen vacancies are created to compensate excess negative charge, reducing the interaction between Co and O [22]. Among the series of $La_{1-x}Sr_xCoO_{3-\delta}$ ceramic materials, the conductivities of LSC64 (88 S $cm^{-1}$) and LSC73 (79 S $cm^{-1}$) are slightly lower than that of LSC55 (95 S $cm^{-1}$). Therefore, we carried out EIS measurements of these three materials for comparison to identify the most promising substrate for supercapacitors.

**Table 1 Lattice parameters of the synthesized $La_{1-x}Sr_xCoO_{3-\delta}$**

| $x$ in $La_{1-x}Sr_xCoO_{3-\delta}$ | Abbreviations | Crystal structure | Space group |
|---|---|---|---|
| 0 | LCO | Rhombohedral | *R*-3*c* |
| 0.2 | LSC82 | Rhombohedral | *R*-3*c* |
| 0.3 | LSC73 | Rhombohedral | *R*-3*c* |
| 0.4 | LSC64 | Rhombohedral | *R*-3*c* |
| 0.5 | LSC55 | Rhombohedral | *R*-3*c* |
| 0.6 | LSC46 | Cubic | *Pm*-3*m* |
| 0.8 | LSC28 | Cubic | *Pm*-3*m* |

As can be seen in Fig. 1(d), the intercept of the semicircle with the real axis and the semi-circle represents the equivalent series resistance (*ESR*, the sum of intrinsic resistance of the LSC, ionic resistance of the electrolyte solution and contact resistance) and the charge transfer resistance ($R_{ct}$), respectively [32]. The Warburg resistance ($R_w$) is associated with the electrolyte ion diffusion [33]. Though the *ESR* of the LSC73 (1.25 Ω $cm^2$), LSC64 (1.17 Ω $cm^2$) and LSC55 (1.13 Ω $cm^2$) are close to each other, their $R_{ct}$ are much different and the corresponding value increases substantially with an increasing $x$ value from 0.3 to 0.5 (as listed in Table. S1). This is because the distorted perovskite oxide structure is unfavorable to fast charge transfer [34, 35]. In consideration of combined electrical conductivities and resistances, LSC73 (i.e. $x = 0.3$) is more suitable as substrate compared with LSC64 and LSC55. Thus, CuO nanoparticles loaded on LSC73 as an electrode for supercapacitors were studied in

further detail.

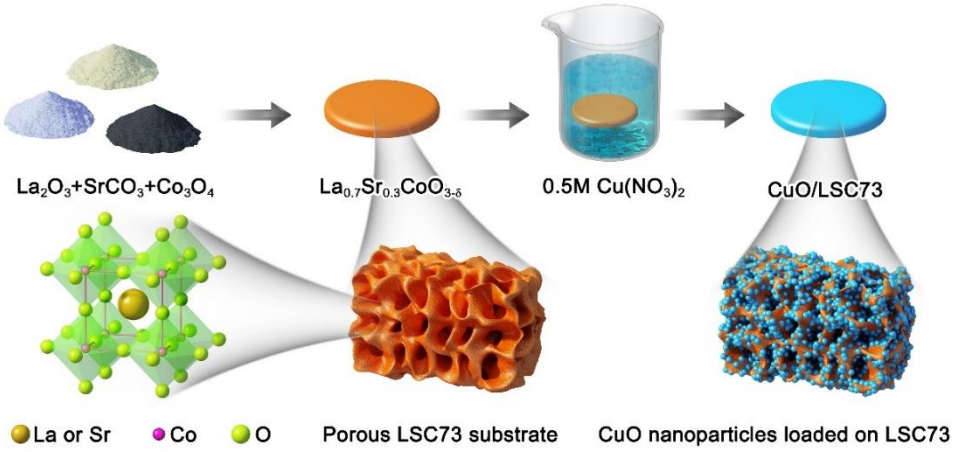


**Figure 2. Scheme of preparation of CuO nanoparticles loaded on porous LSC73.**

Fig. 2 shows the simple steps of CuO/LSC73 preparation. Firstly, the porous LSC73 ceramic substrate was synthesized by a solid-state method (I). CuO nanoparticles with a high mass loading of 10 mg $cm^{-2}$ were then loaded on an LSC73 pellet using infiltration (II) and calcination (III) steps. Fig. 3(a) and Fig. 3(b) show the surface and cross-sectional structure of LSC73, respectively, revealing porous characteristics of the substrate. The CuO nanoparticles distribute evenly on both the surface and internal pore channel of the porous LSC73 substrate, as is displayed in Fig. 3(c and d). Besides, Nitrogen adsorption-desorption measurement was carried out to examine the porous structure of the CuO/LSC73, as shown in Fig. S1. The calculated effective surface area by BET is 6.12 $m^2$ $g^{-1}$. The pore size distributions center at~200 and 300 nm with a relative wide distribution at ~420 nm, which was estimated by BJH, confirming the macrostructure of CuO/LSC73. Fig. 3 (e) shows the TEM image of CuO/LSC73 which further confirms the favorable combination of CuO nanoparticles with a size of ~7 nm on the LSC73 substrate. The high resolution TEM image (inset of Fig 3(e)) displays two lattice spacings of ~0.27 and 0.25 nm, which corresponding to the (104) plane of LSC73 and (002) plane of CuO, respectively. In addition, EDS

mapping analysis is used to identify the element composition and distribution of La, Sr, Co, O and Cu, as shown in Fig. 3(f). The points of Cu are well-distributed in the whole region, adding to the evidence the successful preparation of CuO nanoparticles uniformly loaded on the porous LSC substrate.

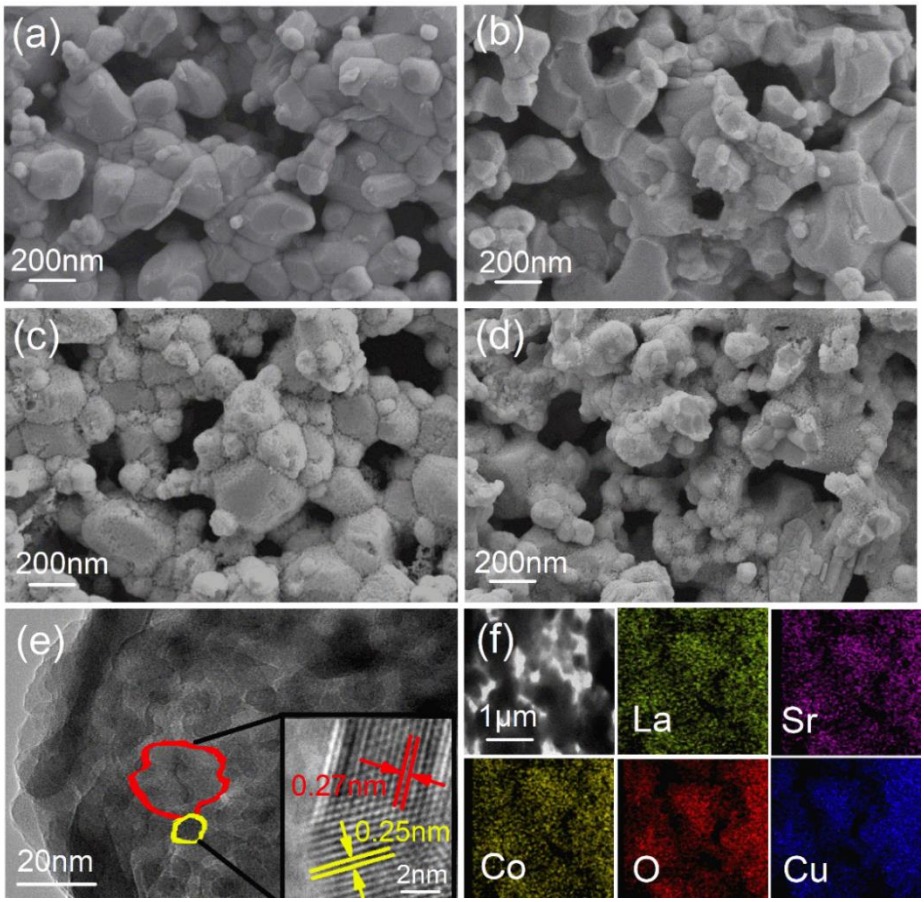


**Figure 3. Surface and cross-sectional SEM images of (a and b) the bare LSC and (c and d) CuO/LSC73. (e) TEM images and (f) EDS element mapping images of CuO/LSC73.**

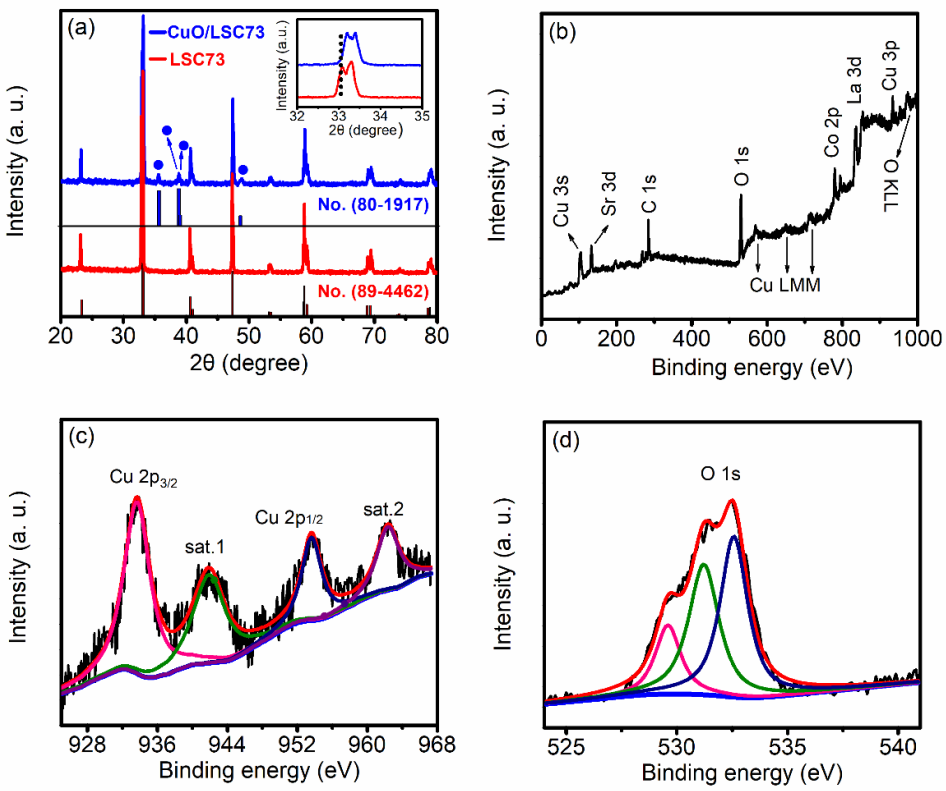


**Figure 4. (a) XRD patterns of the LSC73 and CuO/LSC73. (b) XPS spectrum of CuO/LSC73 of full scan, (c) Cu 2p region and (d) O 1s region.**

Fig. 4(a) shows XRD patterns of the LSC73 and CuO/LSC73 respectively. For the LSC substrate, as displayed in the red line, the diffraction peaks agree well with the standard pattern of the rhombohedral $La_{0.7}Sr_{0.3}CoO_{3-\delta}$ phase (JCPDS card no. 89-4462). Apart from these peaks of LSC73 ceramic substrate, four peaks with cycle symbol at 35.5°, 38.7°, 38.9° and 48.7° can be found in blue, corresponding to (002), (111), (200) and (−202) of the CuO (JCPDS card no. 80-1917), respectively. No extra peaks are detected, suggesting high purity of the prepared product. The element composition and chemical state of the CuO/LSC73 was characterized by XPS. The spectrum in Fig. 4(b) reveals the presence of C (as reference), La, Sr, Co, O and Cu. Fig. 4(c) shows the XPS spectrum of Cu 2p. The peaks at 933.7 and 953.6 eV can be attributed to Cu $2p_{3/2}$ and Cu $2p_{1/2}$, respectively. Furthermore, the shake-up sat.1 and sat.2 peaks confirm the existence of $Cu^{2+}$ in CuO [36]. The fitting O 1s spectrum consists of three peaks, as

shown in Fig. 4(d). The peak at 529.6 eV is typical of metal-oxygen bond, while the other two peaks at 531.2 and 532.6 eV are assigned to hydroxide and absorbed water, respectively [37].

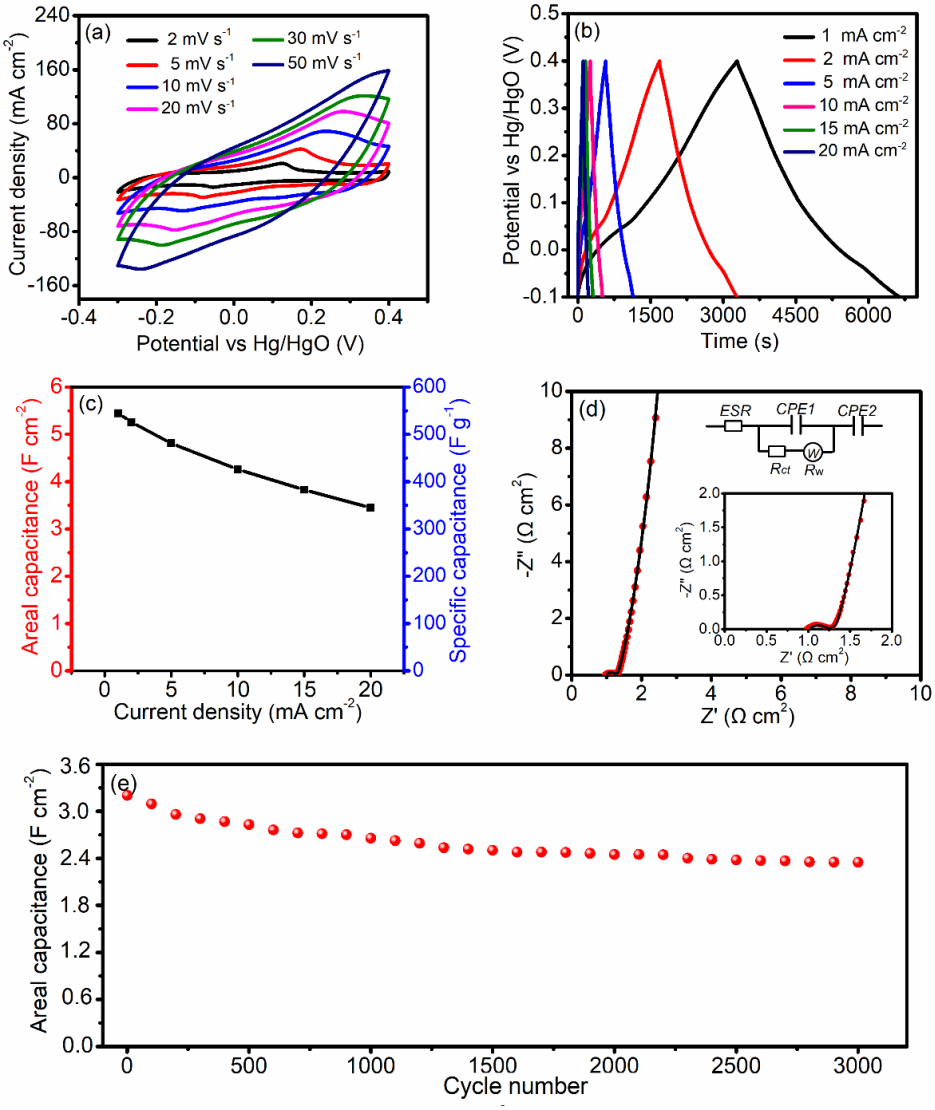


**Figure 5 Electrochemical performance of the CuO/LSC73 electrode: (a) CV curves, (b) GCD profiles, (c) areal capacitance at various current densities, (d) EIS plot (inset: equivalent circuit and enlarged EIS plot) and (e) cycle stability at 20 mA cm$^{-2}$.**

Fig. 5 displays the electrochemical performance of the CuO/LSC73. A wide pair of redox peaks can be found in the CV curves in Fig. 5(a), which are caused by the following reaction in 3.0 M KOH electrolyte solution [38]:

$$2CuO + H_2O + 2e^- \leftrightarrow Cu_2O + 2OH^- \quad (1)$$

$$Cu_2O + H_2O + 2OH^- \leftrightarrow 2Cu(OH)_2 + 2e^- \quad (2)$$

$$CuOH + OH^- \leftrightarrow Cu(OH)_2 + e^- \quad (3)$$

$$CuOH + OH^- \leftrightarrow CuO + H_2O + e^- \quad (4)$$

However, the plateaus in GCD profiles are not obvious, as shown in Fig. 5(b), which may be caused by the incomplete transformation between $Cu^{2+}$ and $Cu^{+}$ and influence of the water splitting reaction [39, 40]. The current produced by the bare LSC is much lower than that of CuO/LSC73 composite as shown in Fig. S2, meaning negligible contribution of the substrate to the capacitance. Fig. 5 (c) shows the areal and specific capacitances at different current densities. The values are 5.45 F $cm^{-2}$ and 545 F $g^{-1}$ at 1 mA $cm^{-2}$, while the areal and specific capacitance are still as high as 3.45 F $cm^{-2}$ and 345 F $g^{-1}$ at 20 mA $cm^{-2}$, respectively, revealing a high rate capability (~63.3% retention) of CuO/LSC73 electrode. The electrochemical performance of CuO/LSC73 is possibly better than previously reported values of CuO-based materials or other transition metal oxides on traditional substrate, as listed in Table 2.

Electrochemical impedance spectroscopy is an important method to evaluate the electrochemical behavior. Fig. 5(d) exhibits the Nyquist plot of the prepared CuO/LSC73. The inset shows the equivalent circuit for fitting the original data and the fitted data are presented in Table S2. The vertical line in the low region means an ideal capacitive property and the Warburg impedance ($R_w$) is associated with fast electrolyte ion diffusion in the porous electrode. In addition, the *ESR* (0.98 Ω $cm^{-2}$) and $R_{ct}$ (0.24 Ω $cm^{-2}$) of the CuO/LSC73 composite are lower than those of LSC73 substrate (1.25 and 0.41 Ω $cm^{-2}$, see Table S1), suggesting positive synergistic effect of CuO nanoparticles and LSC73 substrate. Cycle stability is also evaluated to further

understand capacitive performance of the CuO/LSC73, as shown in Fig. 5(e). After 3000 cycles at 20 mA $cm^{-2}$, the areal capacitance maintains ~74.1%, revealing strong adhesion between CuO nanoparticles and porous LSC substrate. The satisfactory electrochemical performance of the binder-free electrode can be attributed to the porous structure and high conductivity of LSC73, and uniform distribution of CuO nanoparticles, enabling fast electron transfer, ion diffusion and an effective redox reaction.

**Table 2 Comparison of capacitive performance of CuO/LSC73 with previously reported electrode**

| Material/ Substrate | Mass loading (mg $cm^{-2}$) | Nano-structure | Areal capacitance (F $cm^{-2}$) | Specific capacitance (F $g^{-1}$) | Ref. |
|---|---|---|---|---|---|
| CuO/Ni foam | 7 | nanosheet | 3.98 at 5 mA $cm^{-2}$ | 569 5 mA $cm^{-2}$ | [38] |
| CuO/Cu foam | 3.44 | nanorod | 1.67 at 2 mA $cm^{-2}$ | 594.3 2 mA $cm^{-2}$ | [39] |
| $CuMn(OH)_3NO_3$/ Stainless steel plate | 0.775 | nanoparticles | 0.2 at 1 mA $cm^{-2}$ | 258 1 mA $cm^{-2}$ | [41] |
| CuO/Cu foam | 12.2 | nanosheet | 2.6 at 5 mA $cm^{-2}$ | 212 5 mA $cm^{-2}$ | [42] |
| $NiCo_2O_4$/CFP | 7.8 | nanotube | 0.52 at 4 mA $cm^{-2}$ | 66.7 4 mA $cm^{-2}$ | [43] |
| $MnO_2$/Ni foam | 3.0 | dendrites-like | 0.84 at 0.5 mA $cm^{-2}$ | 280 0.5 mA $cm^{-2}$ | [44] |
| $Co_3O_4$/Ni foam | 2.4 | nanowire | 1.24 at 20 mA $cm^{-2}$ | 516.7 20 mA $cm^{-2}$ | [45] |
| CuO/LSC73 | 10 | nanoparticle | 5.45 at 1 mA $cm^{-2}$ | 545 1 mA $cm^{-2}$ | Present |

For comparison, CuO (10 mg $cm^{-2}$) particles were loaded on CFP pellet with a diameter of 1.20 cm via the same method. Fig. S3(a–c) show a typical fiber structure of the bare CFP. Clearly, there are few pores on the surface of the carbon material substrate. Though the morphology of CFP retains well after CuO loading, severe agglomeration of CuO particles is observed, as displayed in Fig. S3(d-f), which is quite different from that of the porous LSC73 with uniformly loading of CuO nanoparticles. Fig. S3(g) shows XRD pattern of CuO/CFP. The sharp diffraction peak at 26.4º is caused by CFP substrate and the other peaks are attributed to CuO (JCPDS No. 80-1917), suggesting high purity of the product. The electrochemical comparisons of CuO/CFP and CuO/LSC73 are conducted at a scan rate of 2 mV $s^{-1}$ and a current density of 10 mA $cm^{-2}$, as seen in Fig S3(h) and (i), respectively. The enclosed area of CuO/LSC73 in the CV curve is much larger than that of CuO/CFP. The former also shows longer discharge time than the latter, implying highly enhanced capacitive performance of CuO loaded on LSC73 compared with CuO on CFP. The highly improved properties could be ascribed to the higher porosity and better wettability of LSC73 than CFP, favoring uniform distribution of CuO nanoparticles on the surface and inner pore of LSC73. Indeed, we also carry out the experiment of CuO on Ni foam through similar steps. However, except for diffraction peaks of Ni and CuO in the XRD pattern, there are distinct peaks of NiO in the final product (in Fig. S4), implying serious corrosion of Ni foam. Through our analysis we claim that, LSC73 could be more suitable as substrate for supercapacitors than traditional substrate CFP and Ni foam.

To verify the practical application of the prepared electrode, a quasi-solid-state asymmetric supercapacitor was assembled which employed CuO/LSC73 as the cathode, CC as the anode and PVA/KOH gel as the electrolyte, respectively. Fig.S5 shows the potential windows of CuO/LSC73 and carbon cloth are -0.3-0.4 V and -1-0 V, therefore

it is expected that the operating voltage for the designed asymmetric supercapacitor can reach to 1.4 V. Shown in Fig. 6(a) is the CV curves of the CuO/LSC73//CC under various potential windows at a scan rate of 50 mV $s^{-1}$, further implying that the stable working potential of the fabricated device can be as high as 1.4 V. The CV curve at different scan rates is presented in Fig 6(b). Obviously, no redox reaction is observed, which belongs to the characteristic of the supercapacitor. The symmetrical lines in charge-discharge curve at various current densities from 10 to 80 mA $cm^{-2}$, offering more powerful evidence for the capacitive nature of the designed device, as seen in Fig. 6(c). The calculated areal capacitances at 10, 15, 20, 30, 40, 50, 60 and 80 mA $cm^{-2}$ are 1.26, 1.20, 1.13, 1.05, 0.97, 0.90, 0.85 and 0.78 F $cm^{-2}$, respectively, as shown in Fig. 6(d). Remarkably, when the current densities increase from 10 to 80 mA $cm^{-2}$, the value of the initial capacitance is only lost 38.0%, implying good rate capability. Fig. 6 (e) shows the long-term stability at a high current density of 50 mA $cm^{-2}$, revealing 98% retention of the initial capacitance after 3500 cycles. Besides, there is a sharp gain of initial areal capacitance from 1 to 100 cycles, as displayed in the inset of Fig 6(e) that is caused by activation of the electrode [46]. However, the areal capacitance becomes lower than the initial value after ~3300 cycles, which may be caused by the inefficient faradic reaction between $Cu^{2+}$ and $Cu^{+}$ at high current density of 50 mA $cm^{-2}$ [15].

Energy density and power density are key parameters to evaluate the overall performance of the CuO/LSC73//CC device and are presented in Fig. 7(a). The device delivers a maximum energy density of 4.92 mWh $cm^{-3}$ with a power density of 99.1 mW $cm^{-3}$ at 10 mA $cm^{-2}$ and a maximum power density of 727 mW $cm^{-3}$ with an energy density of 3.03 mWh $cm^{-3}$ at 80 mA $cm^{-2}$. Interestingly, the obtained values are superior than those of reported supercapacitors, such as PANI /CF//$WO_{3-x}$/$MoO_{3-x}$/CF (0.11 mWh $cm^{-3}$ at 730 mW $cm^{-3}$) [47], $Fe_2O_3$/PPy/CC//$MnO_2$/CC (0.22 mWh $cm^{-3}$ at

165.6 mW $cm^{-3}$) [48], and PEDOT@$MnO_2$@NiNTAs//AC (0.59 mWh $cm^{-3}$ at 84.96 mW $cm^{-3}$) [49] etc. [50-56]. The obtained energy density of CuO/LSC73//CC is comparable to that of lithium batteries (0.3–10 mWh $cm^{-3}$) and higher than that of commercial supercapacitors (< 0.6 mWh $cm^{-3}$) [52]. As displayed in Fig. 7(b), the two CuO/LSC73//CC quasi-solid-state devices in series can drive the LED shining for approximately 20 min after only charging for 1 min.

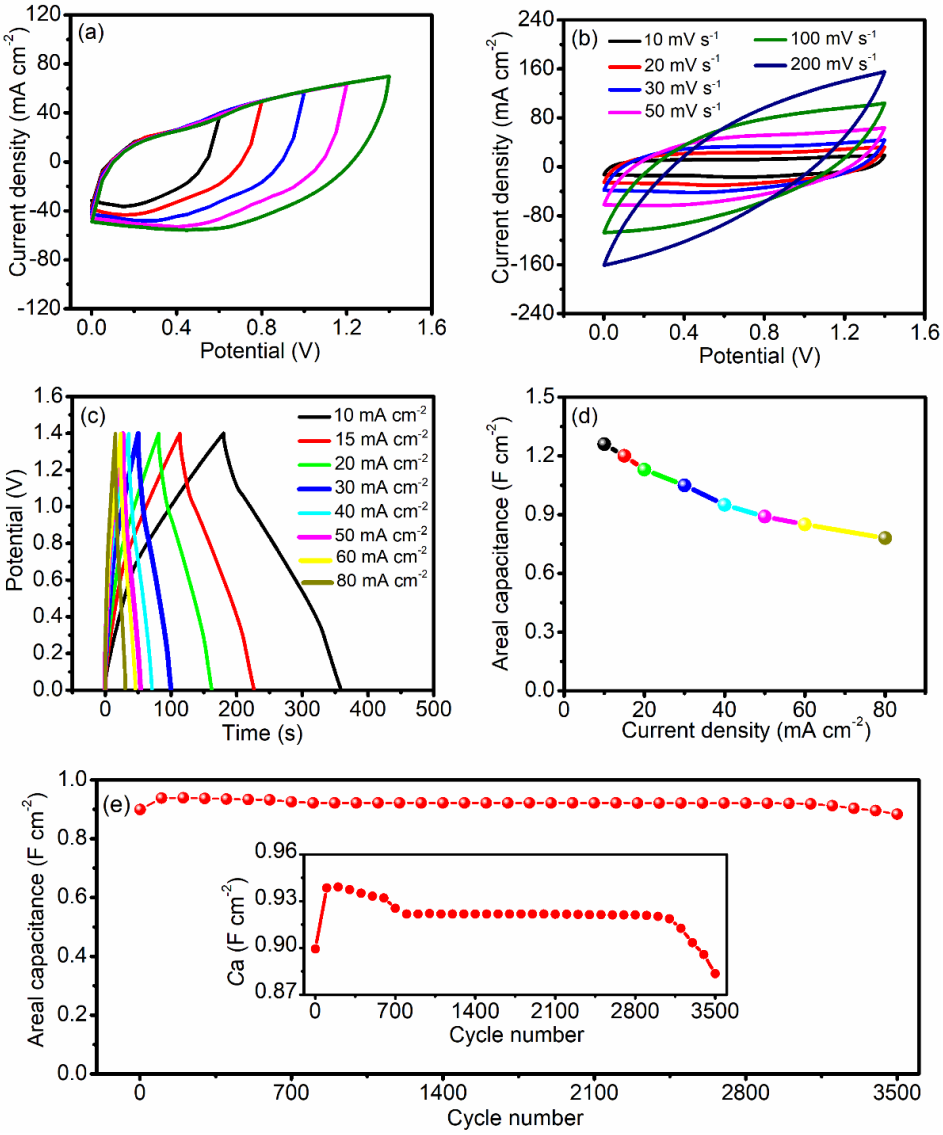


**Figure 6 Capacitive performance of the assembled quasi-solid-state (CuO/LSC73//CC) supercapacitor: (a) CV curves under various potential windows at 50 mV $s^{-1}$; (b) CV profiles at different scan rates; (c) GCD curves at different current densities; (d) areal capacitance; and (e) cycle stability at 50 mA**

**cm$^{-2}$.**

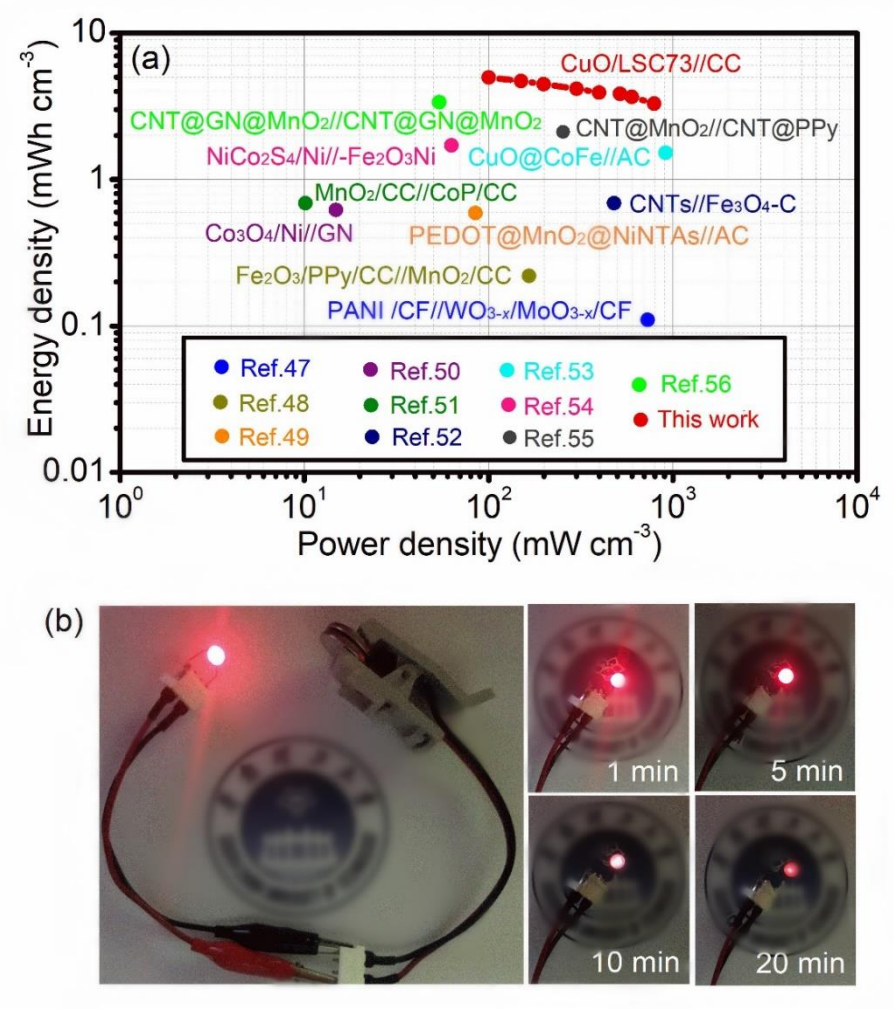


**Figure 7 (a) Ragone plot of the quasi-solid-state asymmetric supercapacitor CuO/LSC73//CC compared with the previously reported supercapacitors and (b) the digital images of LED lighted by the two devices in series.**

To further confirm the superior electrochemical behaviors of the quasi-solid-sate supercapacitor, an aqueous CuO/LSC73//CC device with 3 M KOH solution as electrolyte was assembled for comparison. Fig. S6 (a) and (b) present CV curves at different scan rates and GCD profiles at various current densities of the aqueous supercapacitor, respectively, no obvious redox peaks and charge-discharge platforms are found, suggesting its capacitive nature. The comparison of the two devices in areal

capacitances and impedances are displayed in Fig. S6(c) and (d), respectively. Apparently, the quasi-solid-state CuO/LSC73//CC supercapacitor possesses slightly lower areal capacitance and larger electrochemical impedance than those of the aqueous device, which is resulted from relatively inferior ionic conductivity and poor wettability of PVA/KOH gel [54, 57]. The trivial gap is acceptable with respect to the advantages of the quasi-solid-state device, such as easy package, leak-free and eco-friendliness. The prominent behaviors make the CuO/LSC73 an attractive electrode candidate for energy storage system.

## CONCLUSIONS

A series of porous ceramic material $La_{1-x}Sr_xCoO_{3-\delta}$ ($0 \leq x \leq 0.8$) were synthesized via a solid-state method. The crystal structures and electrochemical properties clearly change with the increase of Sr content ($x$). LSC73 (i.e. $x$ = 0.3) shows comparable electrical conductivity (~79 S $cm^{-1}$) and lower resistance. Therefore, CuO nanoparticles with a high mass loading (10.0 mg $cm^{-2}$) on LSC73 as a binder-free electrode for supercapacitors was investigated. The results revealed that the areal and specific capacitances of the CuO/LSC73 are as high as 5.45 F $cm^{-2}$ and 545 F $g^{-1}$ at 1 mA $cm^{-2}$, respectively. While the current density reached up to 20 mA $cm^{-2}$, the capacitances still remain 3.45 F $cm^{-2}$ and 345 F $g^{-1}$, respectively, revealing good rate capability. The quasi-solid-state asymmetric supercapacitor with CuO/LSC73 as a cathode and CC as an anode exhibited a comparable areal capacitance of 1.26 F $cm^{-2}$ at 1 mA $cm^{-2}$ to that of the aqueous device (1.39 F $cm^{-2}$), satisfying electrochemical performance with high energy density of 4.92 mWh $cm^{-3}$ at a power density of 99.1 mW $cm^{-3}$ and long-term stability (~98% retention of initial capacitance after 3500 cycles at 50 mA $cm^{-2}$) under a wide potential window of 1.4 V. These desirable electrochemical properties can be

attributed to high conductivity and porous structure of LSC substrate and uniformly distributed CuO nanoparticles, ensuring fast electron transfer, ion diffusion and effective redox reaction. Such a favorable and novel electrode CuO/LSC73 could play a vital role in high-performance energy storage systems.

## ASSOCIATED CONTENT

### Supporting Information Available:

*ESR* and $R_{ct}$ comparision, Nitrogen adsorption-desorption isotherm and its corresponding pore size distribution profiles, Electrochemical behaviors of LSC73, Fitted resistances, SEM images, XRD patterns, CV curves, Electrochemical performance of supercapacitor.

## AUTHOR INFORMATION


### Corresponding authors:

*M.N., email: meng.ni@polyu.edu.hk

*J.L., email: jiangliu@scut.edu.cn

### ORCID:

Peipei Liu: 0000-0002-6700-1556 Xiaolin Weng: 0000-0002-9041-3196;

Zhijun Liu: 0000-0002-3949-5501 Yapeng Zhang: 0000-0003-0735-2773;

Qianyuan Qiu: 0000-0002-5993-257X Wei Wang: 0000-0002-3768-8246;

Mingyang Zhou: 0000-0003-1135-2012 Weizi Cai: 0000-0001-9063-5226;

Meng Ni*: 0000-0001-5310-4039 Meilin Liu: 0000-0002-6188-2372;

Jiang Liu*: 0000-0002-8007-1903

## ACKNOWLEDGMENTS

The authors acknowledge the financial support from by Special Funds of Guangdong Province Public Research and Ability Construction (No. 2014A010106008), National Science Foundation of China (NSFC, No. 21276097), Guangdong Innovative and Entrepreneurial Research Team Program (No. 2014ZT05N200) and National Science Foundation of China (NSFC, No. U1601207).

## REFERENCES

[1] Winter, M.; Brodd, R. J. What Are Batteries, Fuel Cells, and Supercapacitors? *Chem. Rev.* **2004,** *104,* 4245-4269.

[2] Lu X. H.; Yu M. H.; Zhai, T.; Wang, G. M.; Xie, S. L.; Liu, T. Y.; Liang, C. L.; Tong, Y. X.; Li, Y. High Energy Density Asymmetric Quasi-Solid-State Supercapacitor Based on Porous Vanadium Nitride Nanowire Anode. *Nano Lett.* **2013,** *13,* 2628-2633.

[3] He, W. D.; Wang, C. G.; Zhuge, F. W.; Deng, X. L.; Xu, X. J., Zhai, T. Y. Flexible and High Energy Density Asymmetrical Supercapacitors Based on Core/Shell Conducting Polymer Nanowires/Manganese Dioxide Nanoflakes. *Nano Energy* **2017,** *35,* 242-250.

[4] Nagaraju, D. H.; Wang, Q. X.; Beaujuge, P.; Alshareef, H. N. Two-Dimensional Heterostructures of $V_2O_5$ and Reduced Graphene Oxide as Electrodes for High Energy Density Asymmetric Supercapacitors. *J. Mater. Chem. A* **2014,** *2,* 17146-17152.

[5] Wu, Z. B.; Pu, X. L.; Ji, X. B.; Zhu, Y. R.; Jing, M. J.; Chen, Q. Y.; Jiao, F. P. High

Energy Density Asymmetric Supercapacitors from Mesoporous $NiCo_2S_4$ Nanosheets. *Electrochim. Acta* **2015,** *174,* 238-245.

[6] Liu, X. M.; Guan, C.; Hu, Y. T.; Zhang, L.; Elshahawy, A. M.; Wang, J. 2D Metal-Organic Frameworks Derived Nanocarbon Arrays for Substrate Enhancement in Flexible Supercapacitors. *Small* **2017,** *14,* 1702641.

[7] Long, B.; Balogun, M-S.; Luo, L.; Qiu, W. T.; Luo, Y.; Song, S.Q.; Tong Y. X. Phase Boundary Derived Pseudocapacitance Enhanced Nickel-Based Composites for Electrochemical Energy Storage Devices. *Adv. Energy Mater.* **2017,** *8,* 1701681.

[8] Jiang, Q.; Kurra, N.; Alhabeb, M.; Gogotsi, Y.; Alshareef, H. N. All Pseudocapacitive MXene-$RuO_2$ Asymmetric Supercapacitors. *Adv. Energy Mater.* **2018,** *8,* 1703043.

[9] Zhang, J. Feng, H. J.; Qin, Q.; Zhang, G. F.; Cui, Y. X.; Chai, Z. Z.; Zheng, W. J. Interior Design of Three-Dimensional CuO Ordered Architectures with Enhanced Performance For Supercapacitors. *J. Mater. Chem. A* **2016,** *4,* 6357-6367.

[10] He, D.; Wang, G. D.; Liu, G. L.; Suo, H.; Zhao, C. Construction of Leaf-Like CuO-$Cu_2O$ Nanocomposites on Copper Foam for High-Performance Supercapacitors. *Dalton Trans.* **2017,** *46,* 3318-3324.

[11] Deng, M. J.; Wang, C. C.; Ho, P. J.; Lin, C. M.; Chen, J. M.; Lu, K. T. Facile Electrochemical Synthesis of 3D Nano-Architectured CuO Electrodes for High-Performance Supercapacitors. *J. Mater. Chem. A* **2014,** *2,* 12857-12865.

[12] Xu, W. N.; Dai, S. G.; Liu, G. L.; Xi, Y.; Hu, C. G.; Wang, X. CuO Nanoflowers Growing on Carbon Fiber Fabric for Flexible High-Performance Supercapacitors. *Electrochim. Acta* **2016,** *203*, 1-8.

[13] Moosavifard, S. E.; El-Kady, M. F.; Rahmanifar, M. S.; Kaner, R. B.; Mousavi, M. F. Designing 3D Highly Ordered Nanoporous CuO Electrodes for High Performance Asymmetric Supercapacitors. *ACS Appl. Mater. Inter.* **2015,** *7*, 4851-4860.

[14] Neagu, D.; Irvine, J. T. S. Structure and Properties of $La_{0.4}Sr_{0.4}TiO_3$ Ceramics for Use as Anode Materials in Solid Oxide Fuel Cells. *Chem. Mater.* **2010,** 22, 5042-5053.

[15] Vohs, J. M.; Gorte, R. J. High-Performance SOFC Cathodes Prepared by Infiltration. *Adv. Mater*. **2009,** *21,* 943-956.

[16] Liu, Y. X.; Dai, H. X.; Deng, J. G.; Li, X. W.; Wang, Y.; Arandiyan, H.; Xie, S. H.; Yang, H. G.; Guo, G. S. Au/3DOM $La_{0.6}Sr_{0.4}MnO_3$: Highly Active Nanocatalysts forThe Oxidation of Carbon Monoxide and Toluene. *J. Catal.* **2013,** *305*, 146-153.

[17] Chen, J. Y.; He, Z. G.; Li, G. Y.; An, T. C.; Shi, H. X.; Li, Y. Z. Visible-Light-Enhanced Photothermocatalytic Activity of $ABO_3$-Type Perovskites For The Decontamination of Gaseous Styrene. *Appl. Catal. B: Environ.* **2017,** 209, 146-154.

[18] Suntivich, J.; May, K. J.; Gasteiger, H. A.; Goodenough, J. B.; Shao-Horn, Y. A Perovskite Oxide Optimized for Oxygen Evolution Catalysis From Molecular Orbital Principles. *Science* **2011,** *334*, 1383-1385.

[19] Zhu, Y. L.; Zhou, W.; Chen, Z. G.; Chen, Y. B.; Su, C.; Tad, M. O.; Shao, Z. P. $SrNb_{0.1}Co_{0.7}Fe_{0.2}O_{3-\delta}$ Perovskite as A Next-Generation Electrocatalyst for Oxygen Evolution in Alkaline Solution. *Angew. Chem.* **2015,** *127,* 3969-3973.

[20] Yamamoto, O.; Takeda, Y.; Kanno, R.; Noda, M. Perovskite-Type Oxides as Oxygen Electrodes for High Temperature Oxide Fuel Cells. *Solid State Ionics* **1987,**

*22*, 241-246.

[21] Bonet, A., Baben, M. T.; Travitzky, N.; Greil, P. High-Temperature Electrical Conductivity of $LaCr_{1-x}Co_xO_3$ Ceramics. *J. Am. Ceram. Soc.* **2016,** *99,* 917-921.

[22] Cheng, X.; Fabbri, E.; Nachtegaal, M.; Castelli, I. E.; Kazzi, M. E.; Haumont, R.; Marzari, N.; Schmidt, T. J. Oxygen Evolution Reaction on $La_{1-x}Sr_xCoO_3$ Perovskites: a Combined Experimental and Theoretical Study of Their Structural, Electronic, and Electrochemical Properties. *Chem. Mater.* 2015, *27,* 7662-7672.

[23] Petrov A. N.; Kononchuk O. F.; Andreev A. V.; Cherepanov V. A.; Kofstad P. Crystal Structure, Electrical and Magnetic Properties of $La_{1-x}Sr_xCoO_{3-\delta}$. S*olid State Ionics* **1995,** *80,* 189-199.

[24] Wu, Y. C.; Huang, P. Y.; Xu, G. Y. Properties and Microstructural Analysis of $La_{1-x}Srx CoO_{3-\delta}$ ($x$=0-0.6) Cathode Materials. *Ceram. Int.* **2017,** *43*, 2460-2470.

[25] Mineshige, A.; Kobune, M.; Fujii, S.; Ogumi, Z.; Inaba, M.; Yao, T.; Kikuchi, K. Metal-Insulator Transition and Crystal Structure of $La_{1-x}Sr_xCoO_3$ as Functions of Sr-Content, Temperature, and Oxygen Partial Pressure. *J. Solid State Chem.* **1999,** *142,* 374-381.

[26] Liu, P. P.; Liu, J.; Cheng, S.; Cai, W. Z.; Yu, F. Y.; Zhang, Y. P.; Wu, P.; Liu, M. L. A High-Performance Electrode for Supercapacitors: Silver Nanoparticles Grown on A Porous Perovskite-Type Material $La_{0.7}Sr_{0.3}CoO_{3-\delta}$ Substrate. *Chem. Eng. J.* **2017,** *328,* 1-10.

[27] Wang, L.; Luo, X. M.; Barbieri, D.; Bao, C. Y.; Yuan, H. P. Controlling Surface Microstructure of Calcium Phosphate Ceramic From Random to Custom-Design. *Ceram. Int.* **2014,** *40*, 7889-7897.

[28] Mai, L. L.; Minhas-Khan, A.; Tian, X. C.; Hercule, K. M.; Zhao, Y. L.; Lin, X.; Xu, X. Synergistic Interaction between Redox-Active Electrolyte and Binder-Free Functionalized Carbon for Ultrahigh Supercapacitor Performance. *Nat. Commun.* **2015,** *6,* 8503.

[29] Mefford, J. T.; Rong, X.; Abakumov, A. M.; Hardin, W. G.; Dai, S.; Kolpak, A. M.; Johnston, K. P.; Stevenson, K. J. Water Electrolysis on $La_{1-x}Sr_xCoO_{3-\delta}$ Perovskite Electrocatalysts. *Nat. Commun.* **2016,** *7*, 11053.

[30] Kozuka, H.; Yamada, H.; Hishida, T.; Yamagiwa, K.; Ohbayashia, K.; Koumoto, K. Electronic Transport Properties of The Perovskite-Type Oxides $La_{1-x}Sr_xCoO_{3\pm\delta}$. *J. Mater. Chem.* **2012,** *22,* 20217-20222.

[31] Efimova, E.; Efimov, V.; Karpinsky, D.; Kuzmin, A.; Purans, J.; Sikolenko, V.; Tiutiunnikov, S.; Troyanchuk, I.; Welter, E.; Zajac, D.; Simkin, V.; Sazonov, A. Short- and Long-Range Order in $La_{1-x}Sr_xCoO_3$ and $La_{1-x}Ba_xCoO_3$. *J. Phys. Chem. Solids* **2008,** *69,* 2187-2190.

[32] Sheberla, D.; Bachman, J. C.; Elias, J. S.; Sun, C-J.; Shao-Horn, Y.; Dinca, M. Conductive MOF Electrodes for Stable Supercapacitors with High Areal Capacitance. *Nat. Mater.* **2017,** *16,* 220-224.

[33] Zhang, X. Y.; Deng, S. J.; Zeng, Y. X.; Yu, M. H.; Zhong, Y.; Xia, X. H.; Tong, Y. X.; Lu X. H. Oxygen Defect Modulated Titanium Niobium Oxide on Graphene Arrays: An Open-Door for High-Performance 1.4 V Symmetric Supercapacitor in Acidic Aqueous Electrolyte. *Adv. Funct. Mater.* **2018,** *28,* 1805618.

[34] Cao, Y.; Lin, B. P.; Sun, Y.; Yang, H.; Zhang, X. Q. Symmetric/Asymmetric Supercapacitor Based on The Perovskite-Type Lanthanum Cobaltate Nanofibers With Sr-Substitution. *Electrochim. Acta* **2015,** *178*, 398-406.

[35] Gwon, O.; Yoo, S.; Shin, J.; Kim, G. Optimization of $La_{1-x}Sr_xCoO_{3-\delta}$ Perovskite Cathodes for Intermediate Temperature Solid Oxide Fuel Cells Through The Analysis of Crystal Structure and Electrical Properties. *Int. J. Hydrogen Energy* **2014,** *39*, 20806-20811.

[36] Li, Y. R.; Wang, X.; Yang, Q.; Javed, M. S.; Liu, Q. P.; Xu, W. N.; Hu, C. G.; Wei, D. P. Ultra-Fine CuO Nanoparticles Embedded in Three-Dimensional Graphene Network Nano-Structure for High-Performance Flexible Supercapacitors. *Electrochim. Acta* **2017,** *234*, 63-70.

[37] Xiao, F.; Yuan, S. J.; Liang, B.; Li, G. Q.; Pehkonen, S. O.; Zhang, T. J. Superhydrophobic CuO Nanoneedle-Covered Copper Surfaces for Anticorrosion. *J. Mater. Chem. A* **2015,** *3*, 4374-4388.

[38] Wang, G. L.; Huang, J. C.; Chen, S. L.; Gao, Y. Y.; Cao, D. X. Preparation and Supercapacitance of CuO Nanosheet Arrays Grown on Nickel Foam. *J. Power Sources* **2011,** *196,* 5756-5760.

[39] Liu, Y.; Cao, X. Y.; Jiang, D. G.; Jia, D. D.; Liu, J. Q. Hierarchical CuO Nanorod Arrays in Situ Generated on Three-Dimensional Copper Foam Via Cyclic Voltammetry Oxidation for High-Performance Supercapacitors. *J. Mater. Chem. A* **2018,** *6,* 10474-10483.

[40] He, D.; Xing, S. X.; Sun, B. N.; Cai, H.; Suo, H.; Zhao, C. Design and Construction of Three-Dimensional Flower-Like CuO Hierarchical Nanostructures on Copper Foam for High Performance Supercapacitor. *Electrochim. Acta* **2016,** *210*, 639-645.

[41] Anandan, S.; Raj, B. G. S.; Emeline, A. V.; Bahnemann, D.; Wu, J. J. Facile Ultrasound Assisted Synthesis of Monodisperse Spherical $CuMn(OH)_3NO_3$ Nanoparticles for Energy Storage Applications. *J. Alloys Compd.* **2017,** *699,* 745-

750.

[42] Li, Y. H.; Chang, S.; Liu, X. L.; Huang, J. C.; Yin, J. L.; Wang, G. L.; Cao, D. X. Nanostructured CuO directly grown on copper foam and their supercapacitance performance. *Electrochim. Acta* **2012,** *85*, 393-398.

[43] Xiao, J. W.; Wan, L.; Yang, S. H.; Xiao, F.; Wang, S. Design hierarchical electrodes with highly conductive $NiCo_2S_4$ nanotube arrays grown on carbon fiber paper for high performance pseudocapacitors. *Nano Lett.* **2014,** *14*, 831-838.

[44] Xiao, K.; Li, J. W.; Chen, G. F.; Liu, Z. Q.; Li, N.; Su, Y. Z. Amorphous $MnO_2$ supported on 3D-Ni nanodendrites for large areal capacitance supercapacitors. *Electrochim. Acta* **2014,** *149*, 341-348.

[45] Cai, D. P.; Wang, D. D.; Liu, B.; Wang, L. L.; Liu, Y.; Li, H.; Wang, Y. R.; Li, Q. H.; Wang, T. H. Three-Dimensional $Co_3O_4$@$NiMoO_4$ Core/Shell Nanowire Arrays on Ni Foam for Electrochemical Energy Storage. *ACS Appl. Mater. Inter.* **2014,** *6,* 5050 -5055.

[46] Zhu, Y. Y.; Cheng, S.; Zhou, W. J.; Jia, J.; Yang, L. F.; Yao, M. H.; Wang, M. K.; Zhou, J.; Wu, P.; Liu, M. L. Construction and Performance Characterization of α-Fe2O3/rGO Composite for Long-Cycling-Life Supercapacitor Anode. *ACS Sustain Chem. Eng.* **2017,** *5*, 5067-5074.

[47] Xiao, X.; Ding, T. P.; Yuan, L. Y.; Shen, Y. Q.; Zhong, Q. Z.; Zhang, X. H.; Cao, Y. Z.; Hu, B.; Zhai, T.; Gong, L.; Chen, J.; Tong, Y. X.; Zhou, J.; Wang, Z. L. $WO_{3-x}$/$MoO_{3-x}$ Core/Shell Nanowires on Carbon Fabric as an Anode for All-Solid-State Asymmetric Supercapacitors. *Adv. Energy Mater.* **2012,** *11*, 1328-1332.

[48] Wang, L. B.; Yang, H. L.; Liu, X. X.; Zeng, R.; Li, M.; Huang, Y. H.; Hu, X. L.

Constructing Hierarchical Tectorum-Like α-$Fe_2O_3$/PPy Nanoarrays on Carbon Cloth for Solid-State Asymmetric Supercapacitors. *Angew. Chem. Int. Edit.* **2017,** *129*, 1125-1130.

[49] Li, X. X.; Deng, X. H.; Li, Q. J.; Huang, S.; Xiao, K.; Liu, Z. Q.; Tong, Y. X. Hierarchical Double-Shelled Poly(3,4-ethylenedioxythiophene) and $MnO_2$ Decorated Ni Nanotube Arrays for Durable and Enhanced Energy Storage in Supercapacitors. *Electrochim. Acta* **2018,** *264*, 46-52.

[50] Wang, X. F.; Liu, B.; Liu, R.; Wang, Q. F.; Hou, X. J.; Chen, D.; Wang, R. M.; Shen, G. Z. Fiber-Based Flexible All-Solid-State Asymmetric Supercapacitors for Integrated Photodetecting System. *Angew. Chem. Int. Edit.* **2014,** *126*, 1880-1884.

[51] Zheng, Z.; Retana, M.; Hu, X. B.; Luna, R.; Ikuhara, Y. H.; Zhou, W. L. Three-Dimensional Cobalt Phosphide Nanowire Arrays as Negative Electrode Material for Flexible Solid-State Asymmetric Supercapacitors. *ACS applied Mater. Inter.* **2017,** *9,* 16986-16994.

[52] Li, R. Z.; Wang, Y. M.; Zhou, C.; Wang, C.; Ba, X.; Li, Y. Y.; Huang, X.T.; Liu, J.P. Carbon-Stabilized High-Capacity Ferroferric Oxide Nanorod Array for Flexible Solid-State Alkaline Battery-Supercapacitor Hybrid Device With High Environmental Suitability. *Adv. Funct. Mater.* **2015,** *25*, 5384-5394.

[53] Li, Z. H.; Shao, M. F.; Zhou, L.; Zhang, R. K.; Zhang, C.; Han, J. B.; Wei, M.; Evans, D. G.; Duan, X. A Flexible All-Solid-State Micro-Supercapacitor Based on Hierarchical CuO@layered Double Hydroxide Core–Shell Nanoarrays. *Nano Energy* **2016,** *20*, 294-304.

[54] Fan, H. L.; Liu, W.; Shen, W. Z. Honeycomb-Like Composite Structure for Advanced Solid State Asymmetric Supercapacitors. *Chem. Eng. J.* **2017,** *326,* 518-

527.

[55] Yu, J. L.; Lu, W. B.; Smith, J. P.; Booksh, K. S.; Meng, L. H.; Huang, Y. D.; Li, Q. W.; Byun, J. H.; Oh, Y.; Yan, Y. S.; Chou, T. W. A High Performance Stretchable Asymmetric Fiber-Shaped Supercapacitor With a Core-Sheath Helical Structure. *Adv. Energy Mater.* **2017,** *7,* 1600976.

[56] Wang, H. M.; Wang, C. Y.; Jian, M. Q.; Wang, Q.; Xia, K. L.; Yin, Z.; Zhang, M. C.; Liang, X. P.; Zhang, Y. Y. Superelastic Wire-Shaped Supercapacitor Sustaining 850% Tensile Strain Based on Carbon Nanotube@Graphene Fiber. *Nano Res.* **2018,** *11*, 2347-2356.

[57] Xu, J.; Wang, Q. F.; Wang, X. W.; Xiang, Q. Y.; Liang, B.; Chen, D.; Shen, G.Z. Flexible Asymmetric Supercapacitors Based upon $Co_9S_8$ Nanorod//$Co_3O_4$@$RuO_2$ Nanosheet Arrays on Carbon Cloth, *ACS Nano* **2013,** *7*, 5453-5462.